# Subsurface emission effects in AMSR-E measurements: Implications for land surface microwave emissivity retrieval

John F. Galantowicz, Jean-Luc Moncet, Pan Liang, Alan E. Lipton, Gennady Uymin, Catherine Prigent, Christopher Grassotti

# Subsurface emission effects in AMSR-E measurements: Implications for land surface microwave emissivity retrieval

John F. Galantowicz,[1] Jean-Luc Moncet,[1] Pan Liang,[1] Alan E. Lipton,[1] Gennady Uymin,[1] Catherine Prigent,[2] and Christopher Grassotti[1,3]

Received 2 December 2010; revised 13 May 2011; accepted 14 June 2011; published 7 September 2011.

[1] An analysis of land surface microwave emission time series shows that the characteristic diurnal signatures associated with subsurface emission in sandy deserts carry over to arid and semiarid regions worldwide. Prior work found that diurnal variation of Special Sensor Microwave/Imager (SSM/I) brightness temperatures in deserts was small relative to International Satellite Cloud Climatology Project land surface temperature (LST) variation and that the difference varied with surface type and was largest in sand sea regions. Here we find more widespread subsurface emission effects in Advanced Microwave Scanning Radiometer-EOS (AMSR-E) measurements. The AMSR-E orbit has equator crossing times near 01:30 and 13:30 local time, resulting in sampling when near-surface temperature gradients are likely to be large and amplifying the influence of emission depth on effective emitting temperature relative to other factors. AMSR-E measurements are also temporally coincident with Moderate Resolution Imaging Spectroradiometer (MODIS) LST measurements, eliminating time lag as a source of LST uncertainty and reducing LST errors due to undetected clouds. This paper presents monthly global emissivity and emission depth index retrievals for 2003 at 11, 19, 37, and 89 GHz from AMSR-E, MODIS, and SSM/I time series data. Retrieval model fit error, stability, self-consistency, and land surface modeling results provide evidence for the validity of the subsurface emission hypothesis and the retrieval approach. An analysis of emission depth index, emissivity, precipitation, and vegetation index seasonal trends in northern and southern Africa suggests that changes in the emission depth index may be tied to changes in land surface moisture and vegetation conditions.

**Citation:** Galantowicz, J. F., J.-L. Moncet, P. Liang, A. E. Lipton, G. Uymin, C. Prigent, and C. Grassotti (2011), Subsurface emission effects in AMSR-E measurements: Implications for land surface microwave emissivity retrieval, *J. Geophys. Res.*, *116*, D17105, doi:10.1029/2010JD015431.

## 1. Introduction

[2] Application of microwave radiometry for atmospheric and surface parameter retrievals and data assimilation over land is complicated by the variety of ways that land surface emission may vary temporally and spatially. Variables affecting emission include soil type, small-scale roughness and topography, soil moisture, surface water, heterogeneity, thermal structure, freeze/thaw, snow, and vegetation. This complexity is in contrast to the ocean surface where emission and reflectivity can be usefully modeled using a handful of known or retrievable parameters such as sensor frequency, polarization, and incidence angle, and ocean surface wind speed and surface temperature [*Wentz and Meissner*, 1999]. Ocean surface emission parameterizations enable secondary retrievals such as atmospheric precipitable water without substantial a priori data constraining local conditions.

[3] The work reported here focuses on the estimation of land surface microwave emissivities in areas where the surface skin temperature does not accurately represent the microwave emission source temperature. In such areas the effective microwave emission depth is large relative to the infrared emission skin depth and the emitting medium (soil, vegetation, etc.) is far from isothermal with depth during parts of the day. As reported by *Moncet et al.* [2011a] (hereafter Moncet11), high-quality microwave emissivities can be retrieved over large portions of the globe using an algorithm in which skin temperature measurements from infrared satellite sensors represent the microwave emission source temperatures. However, across large regions the skin temperature method yields emissivities with systematic negative day-night differences (Figure 1). Furthermore, regions with the largest negative day-night biases correspond generally to arid and semiarid areas where low near-surface

[1] Atmospheric and Environmental Research, Inc., Lexington, Massachusetts, USA.
[2] Laboratoire d'Etudes du Rayonnement et de la Matière en Astrophysique, Observatoire de Paris, CNRS, Paris, France.
[3] Now with I.M. Systems Group, Center for Satellite Applications and Research, NESDIS, NOAA, Camp Springs, Maryland, USA.


0148-0227/11/2010JD015431

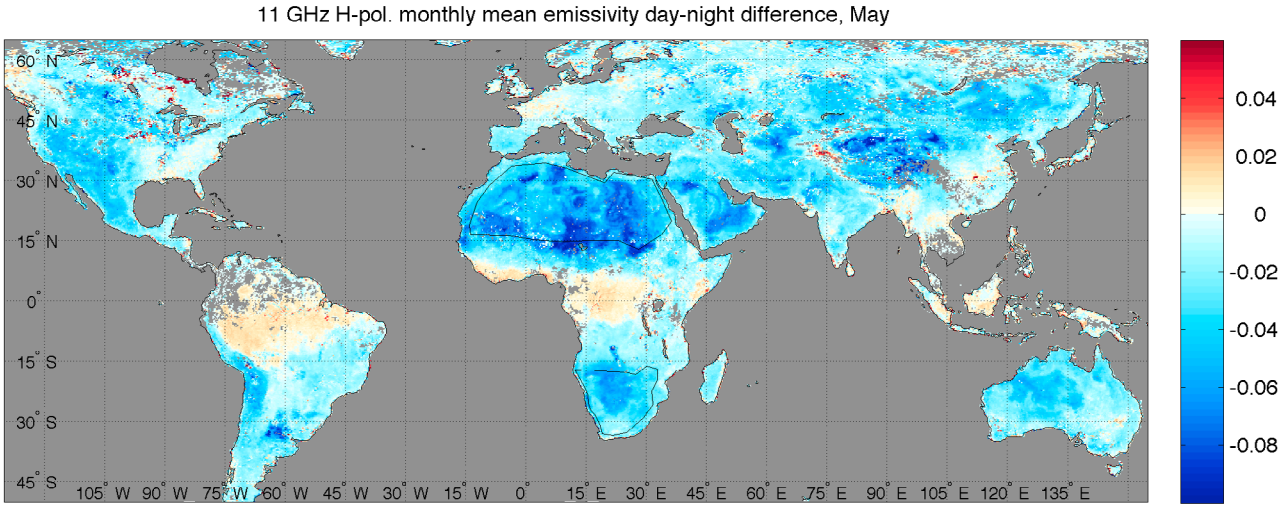


**Figure 1.** The 11 GHz H polarization May 2003 mean day-night emissivity difference from the skin temperature-based retrieval method. The outlines mark regions of northern and southern Africa that are discussed in the text and in Figure 7.

moisture content could be expected to lead to increased transmittance within the surface medium and where emissivities are often diurnally stable due to persistent dryness and minimal vegetation cover. As shown by Moncet11, the occurrence of frequent nighttime dew in humid regions may be the cause of some systematic day-night emissivity differences (observed, for example, in parts of the U.S. during summer months) but these differences are strongly positive. Therefore, the negative day-night differences in arid regions may be attributable primarily to daytime positive and/or nighttime negative biases of the skin temperature relative to the microwave emission source temperature.

[4] The overall objective of the Moncet11 methodology is to derive rigorously quality-controlled land surface emissivities and ancillary parameters in clear-sky conditions. These parameters can be used in cloudy sky conditions to specify a priori constraints for atmospheric and land parameter retrievals within variational retrieval and assimilation systems. Moncet11 discusses the use of lower-frequency brightness temperature indices to monitor surface properties changes and mitigate their effects when clear-sky emissivities are applied in cloudy sky conditions. To account for the effects of subsurface emission, the Moncet11 emissivity retrieval methodology includes an algorithm for the simultaneous retrieval of land surface emissivities and emission depth indices from time series data. The objective of the work reported here was to test the validity of retrievals from the time series algorithm and to begin to examine their sensitivities to spatial and temporal changes in land surface properties.

[5] The Moncet11 process applies the time series retrieval algorithm based on analysis of results from instantaneous retrievals. The instantaneous retrieval method derives 11, 19, 37, and 89 GHz emissivities from temporally coincident brightness temperatures and land surface temperatures from two instruments on NASA's Earth Observing System (EOS) Aqua satellite: the Advanced Microwave Scanning Radiometer-EOS (AMSR-E) and the Moderate Resolution Imaging Spectroradiometer (MODIS) [*Wan*, 1999, 2008]. The process builds upon the prior work of *Prigent et al.* [1997, 1999, 2006] who derived 19, 37, and 85 GHz emissivities using brightness temperatures ($T_B$ or TB) from the Defense Meteorological Satellite Program (DMSP) Special Sensor Microwave/Imager (SSM/I) and land surface temperatures (LST) from the International Satellite Cloud Climatology Project (ISCCP) [*Rossow and Schiffer*, 1999]. The Moncet11 time series process uses a simple one-dimensional heat flow model to solve for vertical and horizontal polarization emissivities and emission depth indices at each AMSR-E frequency over a prescribed model-fitting period (e.g., 1 month) using gridded AMSR-E, MODIS, and SSM/I clear-sky data in a manner similar to *Prigent et al.* [1999] (hereafter Prigent99). Emissivities are assumed to be near constant during the analysis period over which the time series retrieval algorithm is applied.

[6] From the prior work of Prigent99, we know that diurnal variation in SSM/I observations of dry, sandy deserts (i.e., erg landforms) could be explained by the hypothesis of subsurface emission in a transmissive surface media with regular diurnal surface thermal forcing. Other analyses have reinforced the subsurface emission explanation. An analysis of desert surfaces with SSM/I data and simulations showed that thermal emission can originate below the surface at a depth of many wavelengths [*Grody and Weng*, 2008]. Subsurface emission signals from dry sand soils occur at both high and low SSM/I frequencies in addition to well-known volume scattering effects that cause brightness temperatures to decrease as frequency increases [*Grody and Weng*, 2008]. Laboratory-derived microwave penetration depths (i.e., depth of $1/e$ power attenuation) for various rock types and dry soils [e.g., *Ulaby et al.*, 1986] are large enough that diurnally varying subsurface temperature gradients alone may explain the temporal and spectral signatures observed [*Grody and Weng*, 2008]. Diurnal thermal models used for emission from desert soils [Prigent99; *Grody and Weng*, 2008] suggest that the Aqua overpass times (nominally 01:30/13:30 ascending/descending equator crossing times locally) are near the peak of day-night thermal contrast and that subsurface signatures should be observed more widely with AMSR-E data than with SSM/I

(18:30 and 21:00 nominal ascending equator crossing times for the DMSP F13 and F15 satellites).

[7] In this paper we present global monthly analyses of 2003 data showing that diurnal, seasonal, and spatial variations in 11, 19, 37, and 89 GHz AMSR-E observations are well described by the emission depth hypothesis. We first describe derivation of the frequency-dependent emission depth index used in the Moncet11 time series emissivity retrieval algorithm to account for the diurnal effects of subsurface emission from areas in which emissivities may be nearly stable over an analysis period. We compare month-average emission depth indices to patterns of aridity globally and to seasonal cycles and spatial patterns of precipitation and vegetation in northern and southern Africa. We evaluate retrieval quality using time series emission model fit error statistics and analyze retrieval product stability and self-consistency. Finally, we present evidence from data and simulations that subsurface emission (and not, for example, sensor calibration error or processing artifacts) is the dominant source of observed diurnal signals over wide areas of the globe and that the simplified thermal model used in the time series retrieval process can yield emission depth results consistent with a more complex land surface model.

## 2. Time Series Retrieval Methodology

[8] The procedures for retrieving emissivities and emission depth parameters by the instantaneous and time series method are described in detail by Moncet11. This section summarizes the time series retrieval method.

[9] For the first set of processing steps, data from all remote sensing sources were sorted by time and nearest point on a fixed sinusoidal earth grid. Each grid cell was populated at up to six observation times per day corresponding to the Aqua and DMSP F13 and F15 ascending and descending overpass times. Only the first available ascending and descending passes' data from each satellite were recorded since most duplicate (overlapping) passes occur at higher latitudes (>50°) where the time series method is less applicable (Sec. 3). We used V09 AMSR-E Level 2A 10.7, 18.7, 36.7, and 89.0 GHz "resolution 2" TBs, which have been resampled to the 11 GHz native footprint size (51 × 29 km). The common resolution was used to minimize the computational expense of MODIS LST resampling (discussed below). The 6 GHz data were not analyzed for several reasons: they have lower resolution (75 × 43 km), they are more frequently affected by radio frequency interference (RFI), and they are less useful for LST and atmospheric retrieval than the higher frequency channels. Future analyses focused on land surface processes (e.g., soil moisture and vegetation) may include 6 GHz.

[10] Six-hourly atmospheric temperature and water vapor profiles from the 1° National Centers for Environmental Prediction (NCEP) Global Data Assimilation System (GDAS) were interpolated to the overpass times and the AMSR-E and SSM/I footprint centers. Three parameters at each frequency ($\nu$) were calculated from the NCEP atmospheric profiles by radiative transfer along each footprint line of sight: upwelling ($T_\nu^\uparrow$) and downwelling ($T_\nu^\downarrow$) atmospheric emission, which includes the attenuated cosmic background, and total atmospheric transmittance ($\tau_\nu$). MODIS/Aqua Version V004 5 km Level-3 gridded day/night algorithm LSTs (short name MYD11B1 [*Wan*, 1999, 2008]), considered coincident in time with the AMSR-E measurements, were collected for each AMSR-E footprint ellipsoid, quality-controlled via the accompanying quality flags, and spatially averaged to produce a skin temperature estimate, $T_s$. LSTs corresponding to SSM/I footprints are not required in the time series process. AMSR-E and SSM/I TB, $T_\nu^\uparrow$, $T_\nu^\downarrow$, and $\tau_\nu$, and MODIS-derived $T_s$ values were interpolated from their respective swaths to the sinusoidal grid via distance-weighted averaging. The process tested indicators of cloudiness in the swath data based on the MODIS LST quality flags and quality control tests for AMSR-E footprints and temporally and spatially interpolated International Satellite Cloud Climatology Project (ISSCP) cloudiness products for SSM/I. Only data points populated from footprints with at least 20% good-quality points were used in the time series retrieval.

[11] Under the assumptions of spatial homogeneity, specular surface reflectivity, and a nonscattering atmosphere, the measured TB at frequency $\nu$ and polarization $p$ can be modeled as:

$$\begin{aligned} T_{\nu,p}^B &= T_\nu^\uparrow + \tau_\nu\left[\varepsilon_{\nu,p}T_{e,\nu} + \left(1-\varepsilon_{\nu,p}\right)T_\nu^\downarrow\right] \\ &= \left(T_\nu^\uparrow + \tau_\nu T_\nu^\downarrow\right) + \varepsilon_{\nu,p}\left(\tau_\nu T_{e,\nu} - \tau_\nu T_\nu^\downarrow\right), \end{aligned} \tag{1}$$

where $\varepsilon_{\nu,p}$ is the surface emissivity and $T_{e,\nu}$ is the effective temperature of the source of thermal radiation emitted from the surface. Since the atmospheric terms are accounted for using external data sources, we rewrite (1) using the equivalent notation:

$$T_{\nu,p}^B = A_\nu + \varepsilon_{\nu,p}\left(B_\nu T_{e,\nu} + C_\nu\right). \tag{2}$$

From (2) it is clear that accurate $T_{e,\nu}$ estimation is required if $\varepsilon_{\nu,p}$ is to be accurately estimated. If the surface medium is opaque (highly absorbing) or isothermal then $T_s$ is a valid approximation for $T_{e,\nu}$ and consequently $T_{e,\nu}$ is frequency independent (i.e., the gray body approximation applies) and (2) may be readily inverted for $\varepsilon_{\nu,p}$. This approach is applied in the Moncet11 instantaneous emissivity retrieval method.

[12] The time series retrieval method estimates time-average emissivities (per frequency and polarization) and emission depth parameters (per frequency) from data aggregated by time of day over a selected analysis period in a manner similar to that demonstrated by Prigent99. First, typical temperature variation per time of day, $t$, and depth, $d$, is modeled by a solution to the one-dimensional heat-flow equation for a semi-infinite homogeneous medium:

$$\kappa\frac{\partial^2 T(d,t)}{\partial d^2} = \frac{\partial T(d,t)}{\partial t}, \tag{3}$$

where $\kappa$ is the thermal diffusivity of the medium. Under continuous periodic surface heating with 24 h period, the solution to (3) can be expressed as a cosine series:

$$T(\alpha,t) = T_0 + \sum_n A_n \exp\left(-\alpha\sqrt{n}\right)\cos\left(n\omega_0 t + \phi_n - \alpha\sqrt{n}\right), \tag{4}$$

where $\omega_0 = 2\pi/86400$ [$s^{-1}$] and $\alpha = d\sqrt{\omega_0/2\kappa}$ is a non-dimensional depth parameter that damps the cosine wave

amplitudes and shifts their phases relative to the surface waves. At the surface ($\alpha = 0$), (4) simplifies to:

$$T_s(t) = T(0,t) = T_0 + \sum_n A_n \cos(n\omega_0 t + \phi_n). \quad (5)$$

The parameters $T_0$, $A_n$, and $\phi_n$ characterize the periodic surface temperature forcing of the subsurface temperature profile. $T_0$ represents the mean surface (and subsurface) temperature over the time period analyzed, and $A_n$, and $\phi_n$ are the amplitude and phase of the $n$th term in the cosine series representation of the periodic surface temperature. We can take (5) to be a model for typical diurnal variation in infrared emission source temperatures over an analysis period.

[13] Microwave emission from a transmissive surface medium will be a complex function of its spatially varying temperature and radiative properties (e.g., absorption, scattering, refraction). In general the radiative properties are too uncertain to accurately model subsurface radiative transfer from first principles, so we instead seek to model effective emission source temperatures per frequency, $T_{e,\nu}$, that can (1) produce unbiased emissivity estimates via equation (2), (2) account approximately for the range of depths influencing emission, and (3) conform to the subsurface and surface diurnal thermal models, equations (4) and (5). We formulate the model for typical diurnal $T_{e,\nu}$ variation by integrating equation (4) from the top ($\alpha_0$) to the bottom ($\alpha$) of a layer:

$$\begin{aligned} T_e(\alpha_0, \alpha, t) &= T_0 + \sum_n \frac{A_n \exp(-\alpha_0\sqrt{n})}{2\Delta\alpha\sqrt{n}} \\ &\cdot \left[\cos(n\omega_0 t + \phi_n - \alpha_0\sqrt{n}) + \sin(n\omega_0 t + \phi_n - \alpha_0\sqrt{n})\right] \\ &- \sum_n \frac{A_n \exp(-\alpha\sqrt{n})}{2\Delta\alpha\sqrt{n}} \\ &\cdot \left[\cos(n\omega_0 t + \phi_n - \alpha\sqrt{n}) + \sin(n\omega_0 t + \phi_n - \alpha\sqrt{n})\right] \end{aligned} \quad (6)$$

In practice, we set $\alpha_0 = 0$, which yields a one-parameter ($\alpha_\nu$) functional model for $T_{e,\nu}$ ($t$) that defines the frequency-dependent diurnal amplitude and phase relative to $T_s(t)$.

[14] In this study, the parameters in equations (2), (5), and (6) are systematically derived by nonlinear least squares fitting of the models to the time series data arrayed at each grid point and aggregated by time of day over a 1 month analysis period. First, taking only the first two terms in the cosine series (i.e., $n = 1, 2$), we fit equation (5) to the collected SSM/I and AMSR-E 85 and 89 GHz vertical polarization atmospherically corrected TBs, solving for $\{T_0, A_1, A_2, \phi_1, \phi_2\}$. This yields an estimate of the surface phase parameters $\{\phi_1, \phi_2\}$, and $\{T_0, A_1, A_2\}$ are discarded. We derive the phase parameters with 85–89 GHz TBs because they are sampled at six times of day whereas Aqua MODIS LSTs are available at only two times, and 85–89 GHz TBs were found to produce solutions with lower model-data fit errors than 37 GHz. Additional LST data (e.g., from MODIS/Terra) may be included in the process in the future to reduce the reliance on microwave data in this step and the attendant errors introduced by assuming that the phase does not shift between the surface and the microwave emission depth. Next, with $\{\phi_1, \phi_2\}$ held constant, equation (5) is fit to the collected MODIS LSTs, solving for $\{T_0, A_1, A_2\}$ and completing the surface parameter set. Last, per frequency, a set of radiative model parameters $\{\varepsilon_V, \varepsilon_H, \alpha\}$ (V = vertical and H = horizontal polarization) are derived simultaneously by using the parameters to fit the model $T_{e,\nu}$ ($\alpha$, $t$) in equation (6) to sets of instantaneous emission temperature estimates, $T^i_{e,\nu}$, at each polarization calculated by inversion of the radiative transfer model (2) for all clear-sky observation times, $i$, in the analysis period:

$$T^i_{e,\nu} = \frac{1}{B_\nu}\left(\frac{T^B_{\nu,p} - A_\nu}{\varepsilon_{\nu,p}} - C_\nu\right) \quad (7)$$

where $\varepsilon_{\nu,p}$ are the time-average emissivities to be solved for.

[15] V and H polarizations are evaluated together under the assumption that emission depth does not depend on polarization, but SSM/I H polarization data are excluded due to the difference in nominal earth incidence angle relative to AMSR-E (53.1° for SSM/I versus 55° for AMSR-E) and the sensitivity of H polarization TBs to this angle. In each fitting step, we test for and remove outliers relative to the model solution and repeat the model fitting step if any are found. Since 19 GHz TBs are available from both AMSR-E and SSM/I and are less affected by atmospheric effects than 37 and 89 GHz, the 19 GHz parameter set is derived first, followed by 37 and 89 GHz, which are derived with the constraint $\alpha_\nu < \alpha_{19}$. Likewise, 11 GHz parameters are derived with the constraint $\alpha_{11} > \alpha_{19}$, which is needed to avoid aliasing that can occur because 11 GHz data are available at only two times of day (i.e., from AMSR-E only). In practice, neither constraint is frequently invoked in monthly analyses where sufficient clear-sky samples are available.

[16] Moncet11 discuss in detail factors affecting emissivity retrievals and efforts to mitigate possible error sources. Errors in MODIS LSTs due to clouds are minimized by selecting the most cloud-free microwave footprints, by only using footprint with less than 20% detected clouds, and by further filtering residual clouds using temporal spatial standard deviation filter. Errors due to the atmospheric correction terms in equation (7) will be lowest at 11 GHz where the atmospheric transmittance is highest. As a measure of the consistency of LSTs, atmospheric profiles, and AMSR-E measurements, Moncet11 reports that the monthly instantaneous emissivity standard deviation is less than 0.005 over 80% of vegetated surfaces, where emissivity is expected to be stable and the emission depths signature is minimal. This suggests a lower bound of about 1.5 K (i.e., for a 300 K scene) on the estimation error of the effective emitting temperature terms given by equation (7). Errors in the time series retrieval algorithm are likely to be dominated by the assumption of continuous periodic surface heating in the thermal models (5) and (6). Meteorological variation will violate this assumption, producing intraday deviations from periodicity and day-to-day variation in diurnal surface forcing amplitude. These effects are analyzed below using the fit error between effective emission temperature retrievals (7) and the diurnal thermal model (6). The time series model includes the first-order effects of surface energy balance partitioning between latent and sensible heat fluxes by using $\alpha_\nu$ to parameterize the thermal response at depth relative to the surface temperature forcing. For example, when latent heat flux is significant,

diurnal temperature amplitude, subsurface temperature gradients, and effective emission depths should all decrease, leading to lower $\alpha_\nu$ retrievals.

[17] Although equation (6) is a major simplification of $T_e$ for general terrestrial surfaces, tests in the following section show it to be a useful parameterization of temporal and spectral variation even for complex regions (e.g., with heterogeneous land surface cover types). Nevertheless, it remains an open question whether equation (6) is optimal when surface-type data (e.g., vegetation cover, soil) or other ancillary information could be included in the solution. For instance, we start with the assumption that $T_0$, which is derived from surface temperature data, is an accurate diurnal mean temperature at all frequencies, but an additional term accounting for slower synoptic or seasonal scale variation may improve accuracy where emission depths are high. Also, 89 GHz was selected over 37 GHz for estimation of the surface phase parameters $\{\phi_1, \phi_2\}$ based on the stability of results in arid regions where the atmospheric water content is generally lower. In some conditions, residual atmospheric noise at 89 GHz may require that either 37 GHz be used instead or that Terra MODIS LSTs (with 10:30/22:30 equator crossing times) be incorporated in the surface temperature analysis. Tests in which the emissivities and emission depths from the time series method are integrated in secondary retrievals (e.g., for LST or atmospheric parameters) will provide validation data that can be used for further algorithm refinements.

## 3. Global Emission Depth and Emissivity Analyses

[18] The time series retrieval methodology has been applied globally at monthly analysis intervals for the year 2003. Emission depth indices and emissivities are difficult to validate directly due to the lack of comparable ground truth measurements. Here, we evaluate the quality of the products and the process based on self-consistency tests that can reveal problems with the algorithm, its underlying assumptions, or the input data sets.

[19] Initial quality control (QC) metrics and thresholds have been established to decide whether emissivities from the time series method are more reliable than those from the instantaneous retrieval method at any particular grid point. These are discussed in detail by Moncet11. We continue to refine these criteria through experience with the emissivity products. The current QC model recommends time series method emissivities only where the solution method converges, there is no snow cover, spatial variation is low, sufficient numbers of day and night clear-sky samples are available, model fit error is low, and the day-night instantaneous emissivity difference is high. In the following analyses we apply the same selection rules except we include time series method points regardless of day-night instantaneous emissivity difference or model fit error in order to analyze results over a wider range of environmental conditions. Snow covered areas are excluded because the QC model is not yet designed to detect the rapid changes in surface scattering characteristics that can occur due to snowpack metamorphosis. High latitude points are not explicitly excluded but weaker diurnal cycles will typically reduce the amplitude of emission depth signatures resulting in higher retrieval errors.

[20] Figure 2 shows the emission depth model parameter $\alpha$ (hereafter, MEDI, for microwave emission depth index) at 11, 19, 37, and 89 GHz retrieved from May 2003 time series analyses. MEDI decreases systematically with frequency but the global spatial patterns remain consistent. Higher 11 GHz MEDI (or MEDI-11) corresponds globally to high day-night 11 GHz instantaneous emissivity differences (Figure 1) and, like emissivity difference, MEDI is correlated with global aridity patterns and surface cover type [e.g., *Friedl et al.*, 2002]. MEDI is generally highest (e.g., MEDI-11 > 1.5) in the large sand seas of North Africa and Arabia and also in the Taklimakan, Great Sandy, Kalahari, Karakum, and Thar deserts, which is consistent with the earlier findings reported by Prigent99. Moderate MEDI values (e.g., 0.5 < MEDI-11 < 1.5) occur over extensive areas including semiarid areas with a range of vegetation cover and soil types. In other months, MEDI patterns are similar in the most arid regions but there are significant seasonal changes in less arid areas, including, for example, western North America and eastern Asia, where MEDI decreases with the onset of the growing season, and southern Africa, where MEDI increases during the dry season (discussed below). Retrieval coverage also changes seasonally due primarily to snow cover and persistent cloud cover. The occurrence of spurious values in regions with sparse retrieval coverage (e.g., parts of South America in Figure 2 and at high latitudes in other months) are likely due to the failure of the quality control process to detect some conditions for which the time series method is invalid (e.g., proximity to water bodies and cloud-contaminated LST data).

[21] A number of tests have been conducted to support the validity of the time series retrieval method and also provide localized metrics of retrieval efficacy. We use indirect methods such as self-consistency, temporal stability, and relationships to other measured parameters as indirect validation because, as in the early stages of many new remote sensing products, it is not possible to perform direct validation against in situ measurements of emissivity or MEDI. The tests provide substantiation of the qualities of the products globally as a first step toward development of derivative retrievals (such as land surface temperature and precipitable water) that can be directly validated.

[22] The QC model evaluates the root-mean-square of the fit error, $T_{e,\nu}(\alpha, t) - T^i_{e,\nu}$, (Figure 3) at each grid point and for each analysis period using all observations contributing to the time series solution (i.e., cloud-free, nonoutliers). The fit error measures, in part, how well the thermal model parameters and associated emissivities match the underlying physics while also measuring the effects of emissivity instability, residual clouds, spatial heterogeneity, and day-to-day differences in the diurnal thermal cycle. 19 GHz V polarization (19V) fit error is used as an overall metric of model skill because 19V data (1) include SSM/I observations, which are unavailable at 11 GHz, (2) are less likely than 37 or 89 GHz to contain residual atmospheric contamination, and (3) have higher-amplitude diurnal emission depth signatures than 37 or 89 GHz and thus are more easily distinguished from other temporal signatures. Lower 19V fit errors (e.g., <2 K, which is near the range of MODIS LST measurement uncertainty [*Wan*, 2008]) correspond to some of the highest emission depths (Figure 2). Better model fit where emission depth is high may be attributable to several factors: (1) deeper temperatures are more consistent than surface temperature

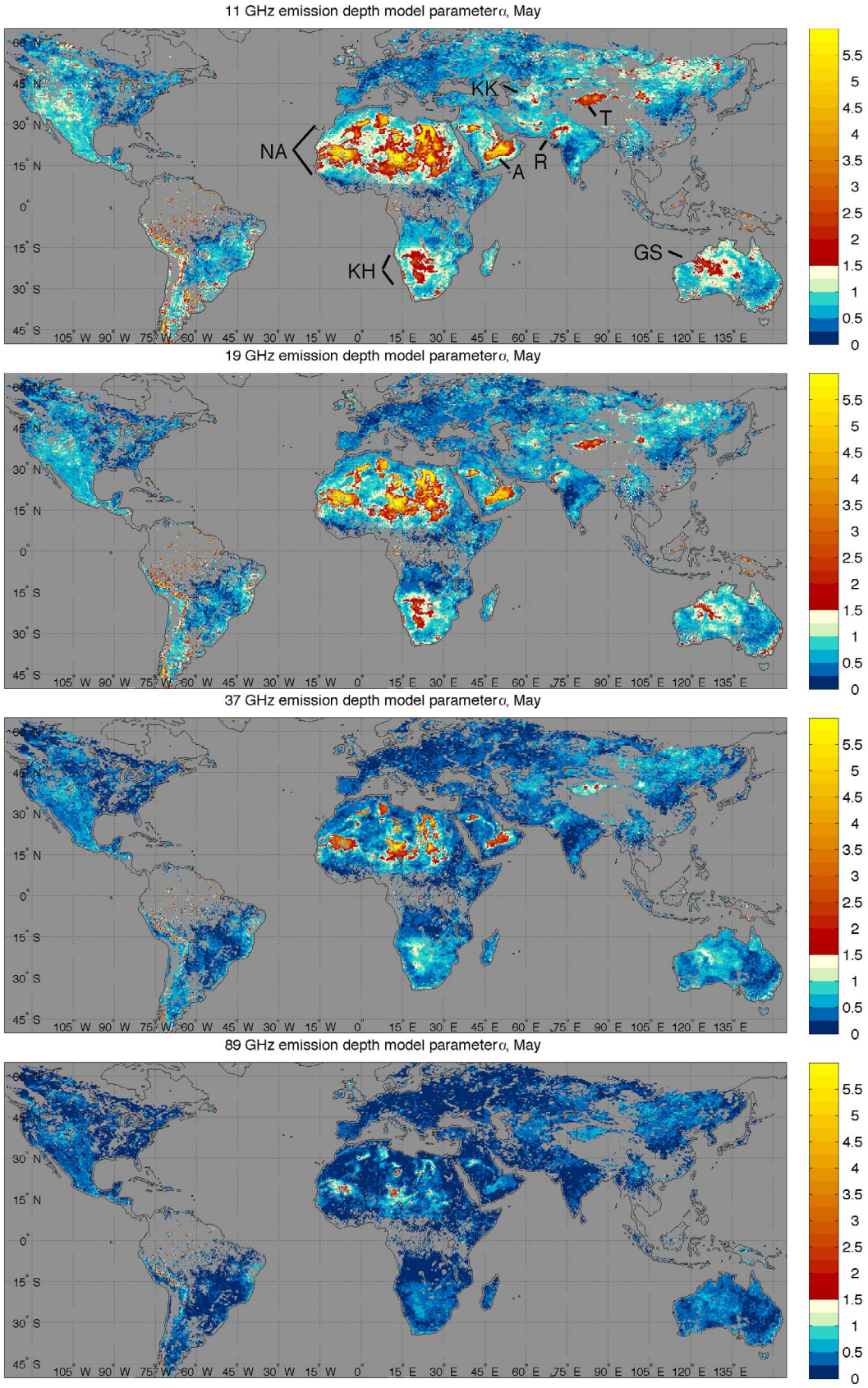


**Figure 2.** May 2003 retrieved emission depth model parameter $\alpha$, or MEDI: (top to bottom) 11, 19, 37, and 89 GHz. Deserts discussed in the text are marked in the top frame: NA, North Africa; A, Arabia; T, Taklimakan; GS, Great Sandy; KH, Kalahari; KK, Karakum; and R, Thar.

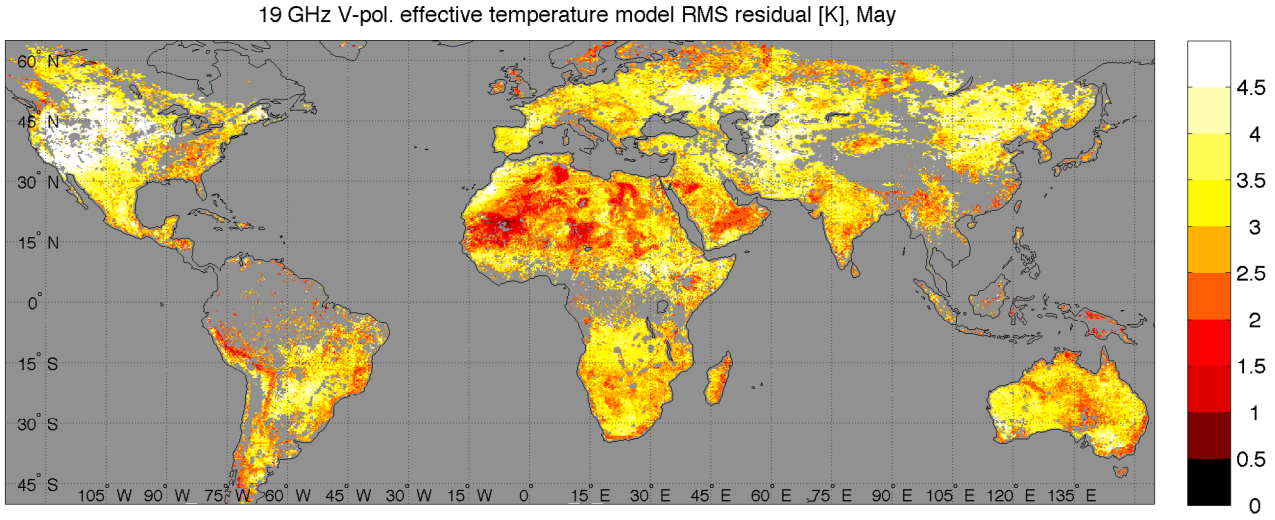


**Figure 3.** Time series model retrieval fit error, $T_{e,\nu}(\alpha, t) - T^{i}_{e,\nu}$, root-mean-square, May 2003, 19 GHz V polarization.

on a day-to-day basis, (2) conditions that promote long periods of aridity and higher emission depth also promote minimal day-to-day changes in vegetation, surface wetness, emissivity, and emission depth, and (3) reduced cloudiness in arid regions promotes more consistent day-to-day surface temperature cycles. In contrast, in May there are higher model fit errors in western North America, where MEDI is lower and surface conditions are likely to be unstable day-to-day due to weather, water, and vegetation changes. As discussed in Moncet11, we are developing methods to use 11 GHz brightness temperature polarization ratio (i.e., V-pol./H-pol.) as a means to detect day-to-day surface changes and isolate periods when emissivities are most stable. This approach will allow the time series retrieval method to be applied to periods that better satisfy the method's emissivity stability requirement than the current fixed monthly analysis increments.

[23] The QC model also tests retrieval model fit error relative to a null-hypothesis alternative in which depth parameter dependence is suppressed (i.e., $\alpha_\nu = 0$). The metric is formulated as an explained variance, i.e., $EV_\alpha = 1 - \sigma^2_\alpha/\sigma^2_{\alpha=0}$, where $\sigma^2$ is the mean square of the fit error, $T_{e,\nu}(\alpha, t) - T^{i}_{e,\nu}$, as discussed above. $EV_\alpha$ measures the fractional reduction in the model's unexplained variance when nonzero penetration ($\alpha$) is allowed as a model solution. Figure 4a shows $EV_\alpha$ for 19 GHz, V polarization data. Generally, where MEDI-19 (Figure 2) is greater than 0.5, 19V $EV_\alpha$ is high (0.5–1.0) and not as spatially variable as fit error (Figure 3), which demonstrates that the time series diurnal model captures a large proportion of the local temporal variability over a month wherever high emission depths are retrieved. $EV_\alpha$ decreases systematically with increasing frequency (Figure 4b), which is consistent with an increase in day-to-day diurnal emission temperature cycle variability expected with decreasing emission depth. However, the persistence of high $EV_\alpha$ regions even at 37 and 89 GHz suggests that the model formulation is suitable for low and high emission depth conditions, and that penetration is a significant factor at these frequencies over substantial areas. High $EV_\alpha$ may also be useful for indicating where MEDI instability can be attributed to factors known to affect emission depth (such as soil moisture or vegetation change) as opposed to the thermal model representation error.

[24] A third test of the retrieval method is through analysis of seasonal variations in MEDI and emissivity. If monthly MEDI is a well-constructed index of emission depth, it should not be affected by month-to-month changes in thermal forcing; it should vary relatively little in continuously dry, barren areas; and it should vary significantly where there are seasonal changes in monthly surface wetness (from very dry to moist) and/or vegetation cover (from predominantly bare ground or dry standing vegetation to predominantly green vegetation). Figure 5a shows the 12 month MEDI-11 range for 2003, excluding months that did not meet the quality control criteria described above (e.g., months with snow cover) and points where fewer than 4 months met the criteria. The largest absolute MEDI-11 range occurs in sand seas where the largest MEDI values occur (Figure 2). More detailed studies are needed to determine if this is due to month-to-month retrieval errors or to actual monthly emission depth variations. Our hypothesis, discussed with further examples below, is that emission depths in these regions may alternate between very large values during drydowns and relatively small values immediately following precipitation. Soil moisture from precipitation will quickly decrease emission depths relative to dry sand and may affect emission depths over a long period due to the amount of time it takes for the sand to return to its driest state throughout the layer from which dry-sand emissions originate. MEDI-11 range is also high in areas of Europe and North America, with MEDI peaking in fall and winter, but this may be due to agricultural practices (i.e., low MEDI occurs at peak growth while high MEDI occurs when crops dry before harvest) or freezing, which may increase near-surface transmittance or cause day-night emissivity change. A strong latitudinal MEDI dependence would indicate that changes in seasonal thermal forcing were affecting MEDI retrieval, but this does not appear to be the case.

[25] Minimum MEDI is zero by definition but the maximum MEDI possible, max($\alpha$), should depend on the local soil and vegetation characteristics. Maximum MEDI may occur,

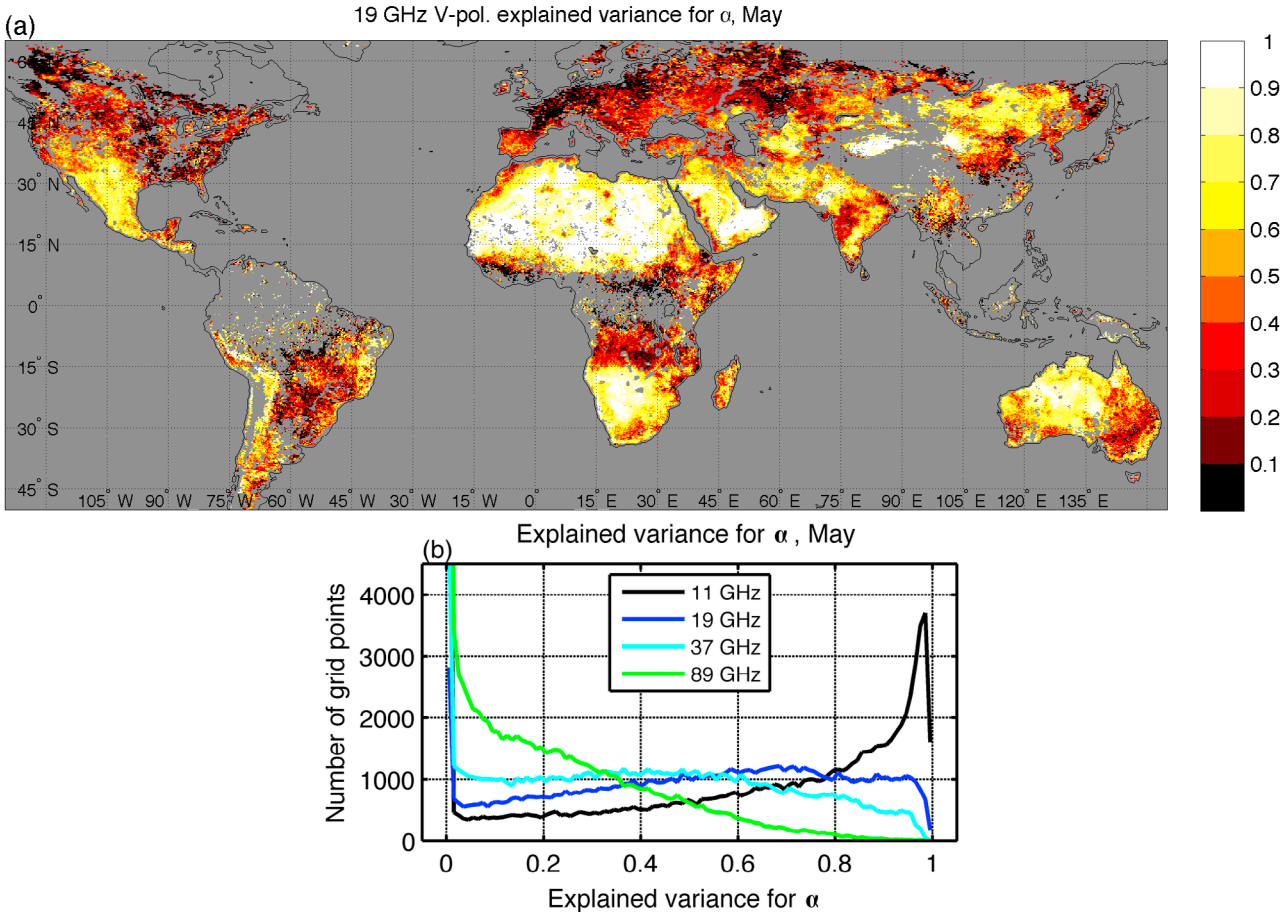


**Figure 4.** Fractional explained variance statistic for the time series model with solution $\alpha$, May 2003: (a) 19 GHz, V polarization and (b) global distribution at 11, 19, 37, and 89 GHz.

for example, only after a long dry spell or vegetation senescence. The normalization $\alpha/\max(\alpha)$ (normalized MEDI or NMEDI) is therefore proposed as an index of emission depth change due primarily to time-varying conditions (e.g., soil moisture, surface water, and vegetation) and isolated from regional differences in surface type. One year is insufficient to determine $\max(\alpha)$ everywhere, so we take 1.5 as a lower limit and normalize $\alpha_{11}$ by the larger of 1.5 or the 2003 maximum $\alpha$. Figure 5b shows $\alpha_{11}/\max(\alpha_{11})$ annual range for 2003. Unlike MEDI, the range in NMEDI-11 is less strongly correlated to surface types like sand seas. In Africa, for example, NMEDI-11 range is larger in areas of the Sahel and parts of southern Africa (places where there is significant seasonal variation in vegetation and wetness) than in the Sahara. In the United States, NMEDI-11 range is generally lower in the western half, which is more arid than the east and therefore has less significant seasonal moisture and vegetation cycles, particularly when months with snow cover are excluded.

[26] Some of the patterns in NMEDI range are similar to those in the annual range of 11 GHz H polarization (11H) emissivity from the time series method (Figure 5c). In Africa, for example, the retrieval produces a narrow range of emissivities in barren areas (e.g., the Sahara) and in permanently vegetated areas where little variation is expected. Like NMEDI, emissivity should respond to strong vegetation and wetness variations, but while MEDI should typically decrease with either increasing wetness or vegetation amount, H polarization emissivity will typically decrease with surface wetness but increase with vegetation.

[27] The differing effects of surface wetness and vegetation on MEDI and emissivity can be seen in comparisons of monthly results from northern and southern Africa. Figure 6 plots the monthly mean and 68% range of four sets of parameters collected in the polygons shown in Figures 1 and 5: 11 GHz $\alpha/\max(\alpha)$ (NMEDI); Tropical Rainfall Measuring Mission (TRMM) monthly precipitation [*NASA*, 2009a]; MODIS Normalized Difference Vegetation Index (NDVI, [*Huete et al.*, 2002; *NASA*, 2009b]); and 11 GHz H and V polarization time series method emissivities. To avoid monthly sampling biases, the analysis only includes points with MEDI retrievals in every month. Figure 7 shows maps of these parameters for the southern Africa region and for three key months: February, May, and September.

[28] In southern Africa, the typical wet season is October through April, and the 2003 TRMM monthly rainfall is near zero across the region from May through September (e.g., see Figure 7). Mean NDVI begins to increase in October, reaches a peak in February, and then decreases gradually throughout the dry season. NDVI generally has high spatial variability across the region but becomes more uniform in September at the end of the dry season (Figure 7), the exception being the Okavango Delta (center top of the

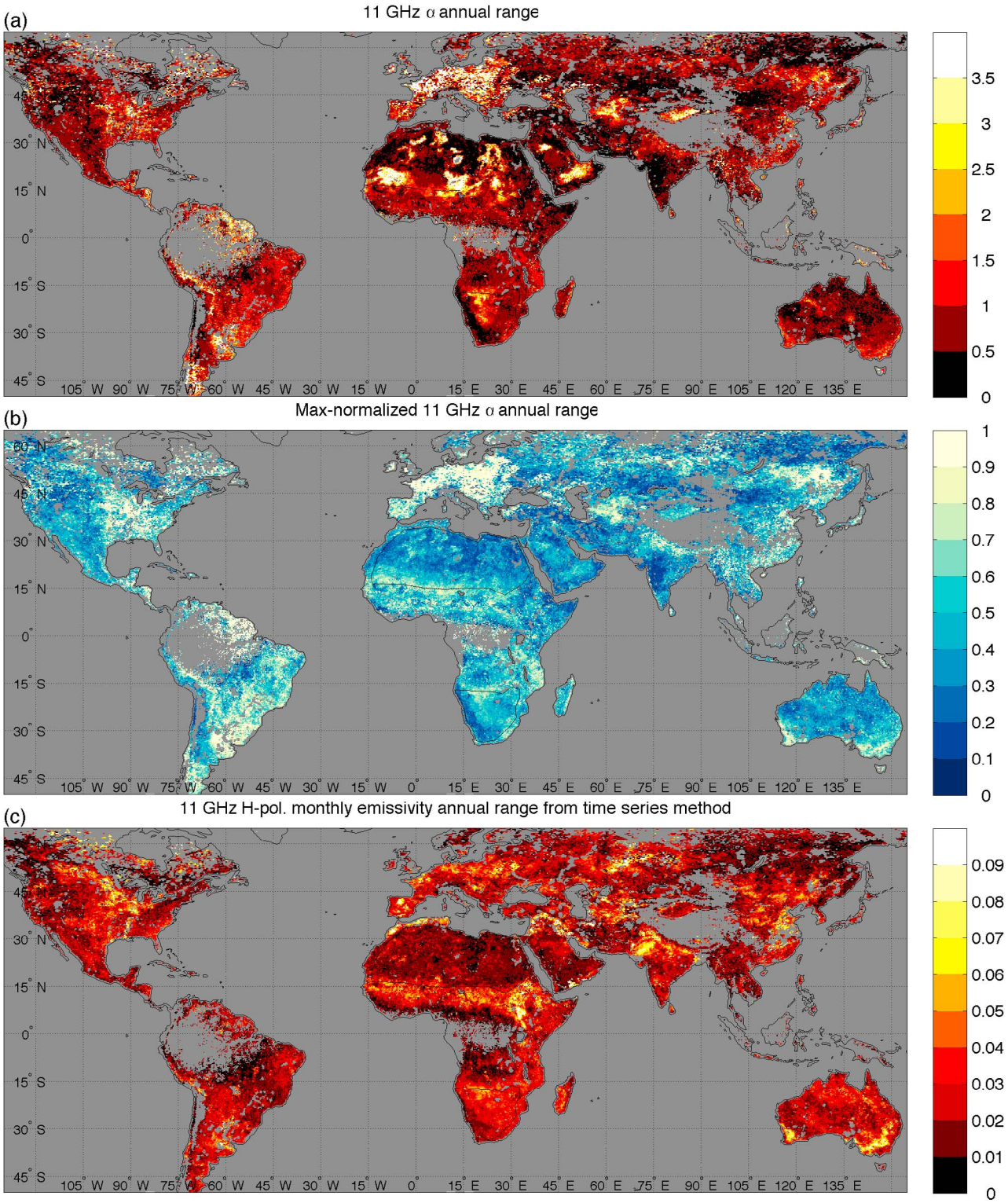


**Figure 5.** The 11 GHz time series retrieval method 2003 annual ranges of (a) $\alpha$ parameter, (b) $\alpha$/max($\alpha$), and (c) H polarization emissivity.

polygon), which the time series method quality control excludes. Mean NMEDI-11 is lowest (0.54) at the wet season peak in February and climbs in March through September to 0.80, roughly following the seasonal cycles of moisture and vegetation. We interpret the gradual increase during the dry season as a response to soil drying and vegetation senescence, both of which should increase near-surface microwave transmittance and vertical temperature gradients. The large NMEDI-11 decrease (0.80 to 0.64) between October and November of appears to be due to increasing surface

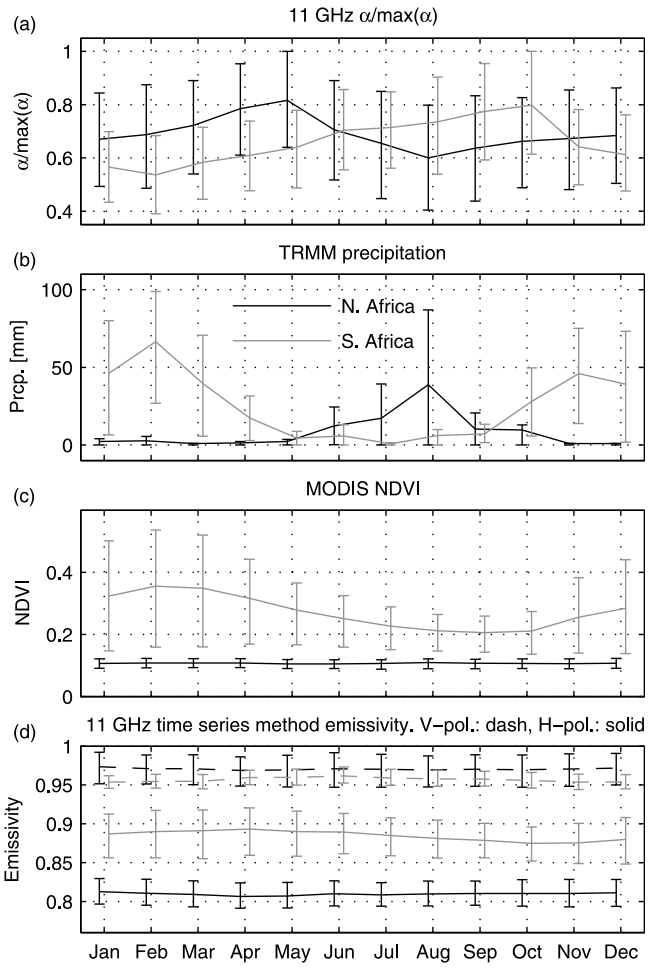


**Figure 6.** Monthly mean and 68% bounds of parameters from the northern (N = 11307) and southern (N = 3334) Africa polygons shown in Figures 1 and 5: (a) 11 GHz $\alpha$/max($\alpha$), (b) monthly precipitation from TRMM, (c) MODIS NDVI, and (d) 11 GHz H and V polarization time series method emissivities.

moisture at the onset of the rainy season and not increasing vegetation amount, which changes relatively slowly. In contrast to NMEDI-11, emissivity changes very little at the onset of the rainy season and overall its seasonal cycle indicates a closer link to vegetation amount than surface moisture. Spatial patterns (Figure 7) tell a similar story: during the dry spell from May through September, NMEDI increases most in the region's center, where both precipitation and NDVI are low, whereas the monthly 11H emissivities appear to correspond to NDVI alone.

[29] In contrast to southern Africa, the northern Africa polygon has consistently low NDVI (~0.1, Figure 6) yet average NMEDI-11 still declines during the weaker rainy season (June–October) to 0.60 and rises gradually during the driest season (November–May) to 0.82. Since there is no strong NDVI cycle, we interpret the NMEDI-11 change in northern Africa as largely a response to changes in soil moisture conditions within the depth of soil that may influence emission. To test this idea, we separately analyzed two subsets of points in the northern Africa polygon: one with maximum monthly precipitation, $P$, greater than 40 mm ($P_{max} > 40$, N = 3945) and one with $P_{max} < 10$ (N = 3460). To minimize vegetation effects, we restricted each set to points with maximum NDVI less than 0.2. The $P_{max} > 40$ set had the same seasonal cycle as the overall region, with average NMEDI-11 reaching a maximum of 0.81 in May but falling to a lower minimum of 0.54 in August. In contrast, the $P_{max} < 10$ set had a reduced seasonal cycle, with NMEDI-11 rising to 0.83 in May but going only as low as 0.71 and staying in the 0.71 to 0.73 range November through March. This result reinforces the conclusions that NMEDI is responding to the seasonal cycle of precipitation and soil moisture and not to seasonal changes in surface thermal forcing.

## 4. Diagnosis of Emission Depth Phenomenology

[30] The time series retrieval method is based on the assumption that emission depth and heat transfer effects are the main drivers of the differences between the diurnal cycles of skin temperature and TB seen in arid regions. The retrieval model fit error tests described above confirm that the model can explain the observations over differing microwave frequencies, polarizations, diurnal cycle amplitudes, surface types, and seasons. In this section we discuss tests that are independent of the retrieval model that also point to an emission depth explanation of the observations and rule out other phenomenon that may be suspected of inducing similar signals.

### 4.1. Surface Type and Calibration

[31] A strong association between day-night brightness temperature difference patterns and surface type can be used to argue against the alternative hypothesis that day-night differences are due to AMSR-E calibration problems. Global uncertainties in the V09 AMSR-E Level 2A TBs used here are considered well established via tests with independent measurements [*Ashcroft and Wentz*, 2006] so any candidate calibration issue would also have to be one that could have been missed by these tests. TB calibration bias with a day-night cycle could arise if an error depended on ascending and descending passes asymmetrically (e.g., due to solar illumination of the instrument) or on TB magnitude (e.g., due to receiver nonlinearity) [*Kunkee et al.*, 2008]. Global patterns interpreted here as related to emission depth are also correlated to regions with high daytime temperatures and large day-night temperature differences, so tests are warranted to rule out calibration as a significant factor.

[32] Figure 8 shows daytime 11V TBs from two sources: (1) measured by AMSR-E and (2) projected from nighttime emissivity and daytime skin temperature estimates, i.e., $\varepsilon$ (night)·$T_s$(day), where $\varepsilon$ (night) is derived by inverting (1) with $T_e = T_s$ (the instantaneous retrieval method). Data are plotted from three regions with different surface types but with comparable TB range and likelihood for day-night emissivity stability (i.e., heavily vegetated or dry region). In the absence of day-night calibration issues, there should be a one-to-one relationship between projected and measured TBs everywhere that emissivity is stable and emission depth is not a factor. In fact, we see that (1) only the Central Russia data set has nearly a one-to-one relationship and (2) the savannah and desert data are systematically offset and by distinctly different amounts. These differences fit

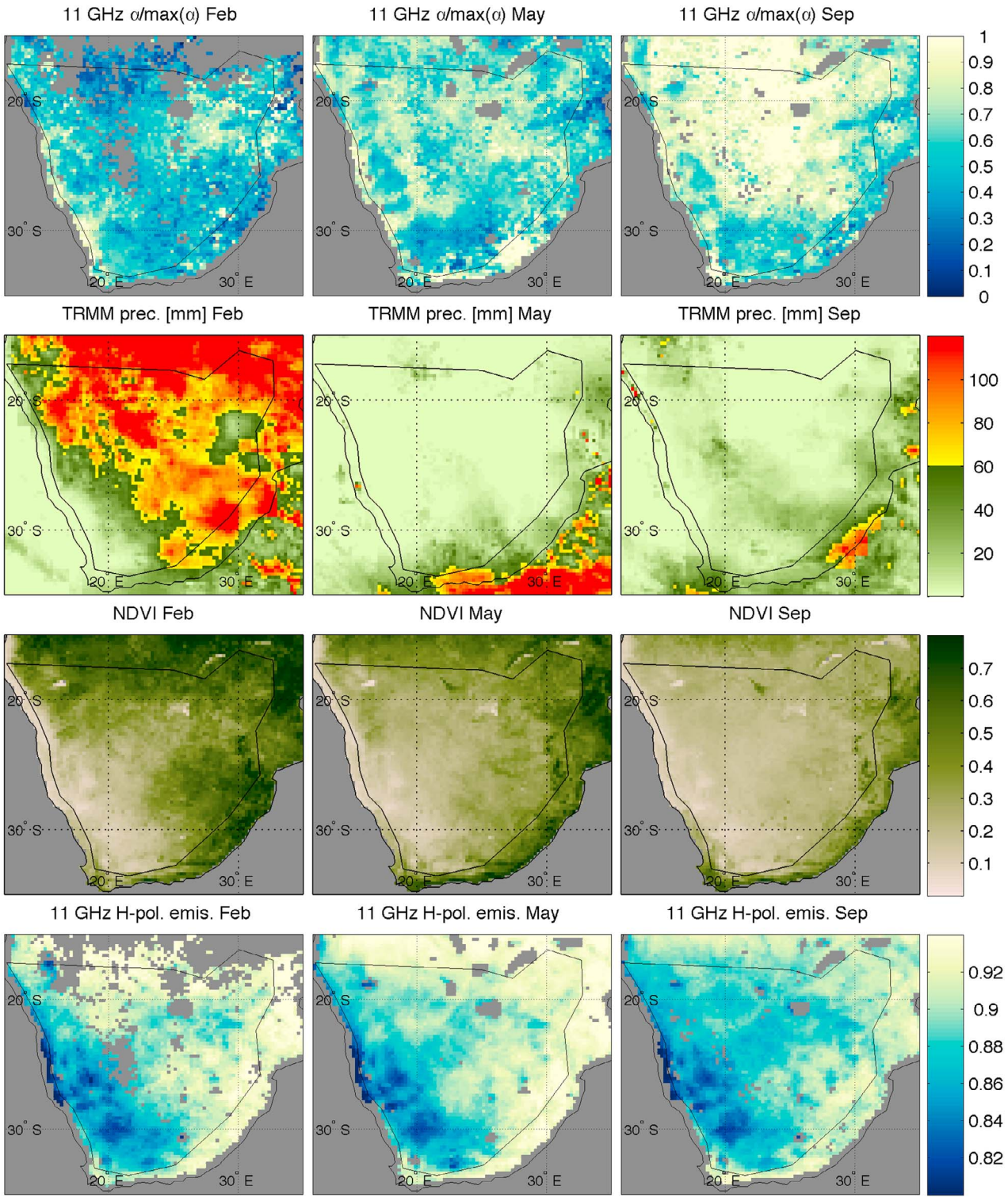


**Figure 7.** (left) February, (middle) May, and (right) September 2003 (top to bottom) 11 GHz $\alpha$/max($\alpha$), TRMM total precipitation, MODIS NDVI, and 11 GHz H polarization emissivity. Emissivity and $\alpha$ are from time series method retrievals. Gray indicates areas that did not pass time series method quality control.

the emission depth hypothesis: the Russia region, which is dominated by presumably low emission-depth temperate forests, has $T_e \approx T_s$ whereas in the progressively drier savannah and desert regions, which presumably have higher emission depths, $T_e$ increasingly diverges from $T_s$ at the midday and midnight observation times. The one-to-one relationship in the Russia region also implies that day-night and TB-correlated calibration issues are negligible (or, less likely, that they are offset by some other factor in this region alone).

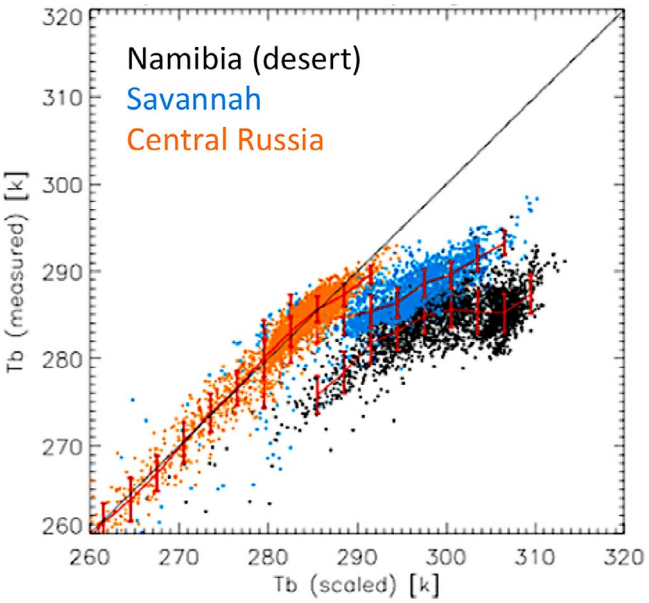


**Figure 8.** Daytime measured 11V TB versus TB predicted from nighttime emissivity retrieval, $\varepsilon$(night) · $T_s$(day), for three regions: Namibia (desert), African savannah, and Central Russia (forest).

[33] Spatial patterns in the day-night difference of the 19V/11V TB ratio (Figure 9) reinforce the conclusion that surface type and vertical temperature gradients are the dominant cause of day-night differences in arid regions globally. Arid regions where this pattern strongly occurs include western North America below 45°N, South America south of the Amazon, North and South Africa, the Middle East, South Central Asia, and Australia. Large day-night 19V/11V changes in other areas, such as the Tibetan Plateau and areas of northern latitudes, are likely due to changes in snow cover or soil freeze/thaw cycles, which we do not address. Neglecting atmospheric effects, the day-night difference can be expressed as $\frac{\varepsilon_{19}^D T_{19}^D}{\varepsilon_{11}^D T_{11}^D} - \frac{\varepsilon_{19}^N T_{19}^N}{\varepsilon_{11}^N T_{11}^N}$ (where $T = T_e$) or, assuming emissivities are constant, $\frac{\varepsilon_{19}}{\varepsilon_{11}}\left[\frac{T_{19}^D}{T_{11}^D} - \frac{T_{19}^N}{T_{11}^N}\right]$. The second formulation is positive if the 11–19 GHz $T_e$ slope is smaller at night than in the daytime; if $T_e$ is frequency-independent day and night, the ratio difference is approximately zero. Assuming $d_{11} > d_{19}$, where $d$ is effective emission depth, the 19V/11V TB ratio will be lower where nighttime $T_e$ increases from $d_{19}$ to $d_{11}$ and higher where daytime $T_e$ decreases from $d_{19}$ to $d_{11}$. The prevalence of positive day-night slope differences in Figure 9 over all major arid regions is consistent with the assumptions of constant day-night emissivities, $d_{11} > d_{19}$ and temperature gradients that would be expected under strong diurnal thermal forcing. Furthermore, nighttime 19V/11V is less than one in many areas, while daytime 19V/11V is almost universally greater than one. Whereas this reversal of the 11–19 GHz spectral slope is consistent with the emission depth hypothesis, it cannot be alternatively explained as a calibration error without hypothesizing severe nonlinearities in receiver response.

[34] An apparent contradiction in the day-night 19V/11V TB difference map can also be explained by the emission depth model. Some sand desert regions (e.g., the Sahara's Marzuq Sand Sea, point A in Figure 9), where emission depth is expected to be largest, have near-zero day-night 19V/11V TB differences, which is the signature expected from surfaces with negligible emission depth. However, as the diurnal temperature "wave" propagates down (e.g., equation (4)) its amplitude decreases and its phase lags in time relative to the surface. Consequently, the depth dependence of the temperature profile at midday and midnight may be less linear at some depths even if it is nearly linear just below the surface. Assuming that both $d_{19}$ and $d_{11}$ are relatively large in dry sand, the $d_{19}$ to $d_{11}$ temperature difference may decrease in magnitude or even change sign relative to the surface gradient. Hence, the occurrence of near-zero day-night TB ratio differences can be attributed to conditions where the $d_{19}$ to $d_{11}$ temperature difference is coincidentally near zero both day

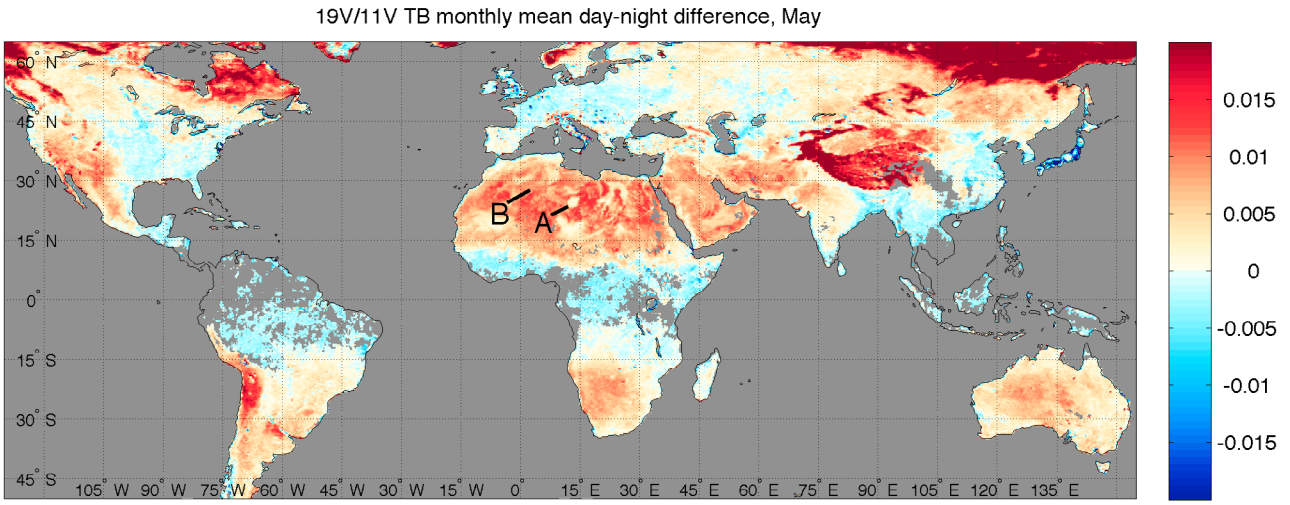


**Figure 9.** May 2003 mean 19/11 GHz V polarization brightness temperature ratio day-night difference. Marks indicate the "sandy desert" (A, 25°N 13°E, in the Marzuq Sand Sea) and "rocky desert" (B, 28°N 3°E) points discussed in sections 4.1, 4.2, and 4.3.

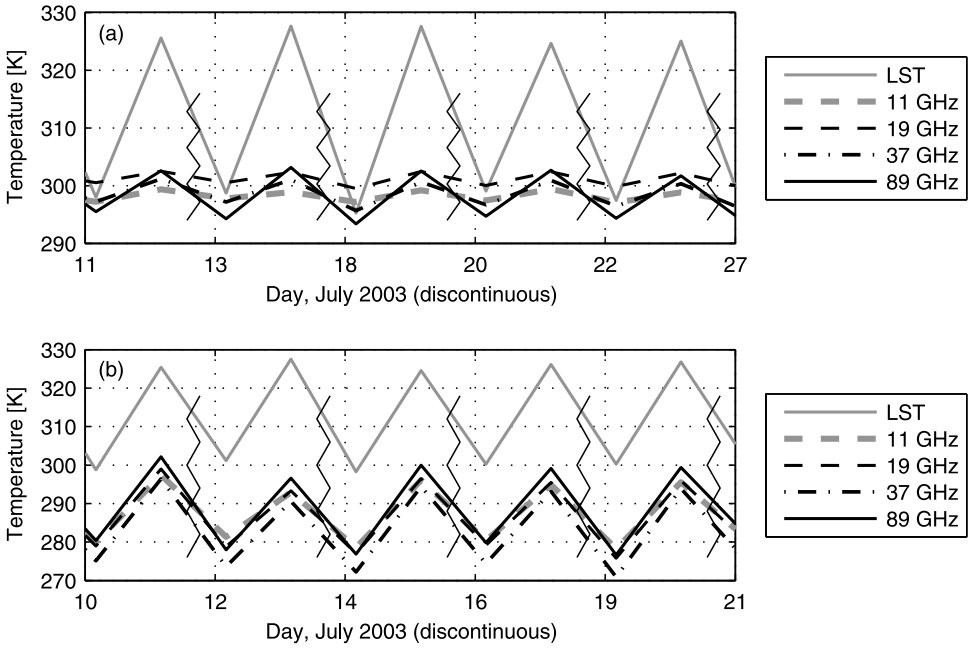


**Figure 10.** MODIS LST and AMSR-E V polarization TB day-night sequences, July 2003, for the (a) "sandy desert" and (b) "rocky desert" grid points in Figure 9. Jagged vertical lines mark 1–2 day discontinuities.

and night or, less likely, the day and night temperature ratios are equal but nonzero. Land surface modeling experiments (described in section 4.3) illustrate the development of these conditions in a simulated dry sand soil.

### 4.2. LST and TB Day-Night Patterns

[35] The emission depth hypothesis can be used to explain patterns in LST and TB day-night sequences and their dependence on surface type. Figure 10 illustrates night-day sequences of LST and TB for Saharan "sandy desert" (point A in Figure 9) and "rocky desert" (point B) surface types. The night-day data pairs are discontinuous due to irregular satellite sampling but, for illustration purposes, are assumed to be representative of continuous data due to their day-to-day consistency. First, at both locations the diurnal amplitude decreases with decreasing microwave frequency and between LST and 89 GHz TB, but the drop is much more pronounced at the sandy site. This finding is consistent with $\alpha$ dependence in the thermal model amplitude term (i.e., $A_n \exp(-\alpha\sqrt{n})$, equation (4)). Second, TBs are offset from LSTs on average, as would be expected from microwave emissivities less than one, but nighttime TBs are not offset as much and in some cases are higher than LST at the sandy site. Atmospheric effects can be ruled out because the rocky and sandy sites have similar atmospheric conditions and because TB > LST occurs more often in channels where atmospheric effects are lowest (11 and 19 GHz). An emissivity effect would be unlikely to have the necessary diurnal cycle in a dry, barren region and, furthermore, emissivities greater than one would be needed. The relatively high nighttime TBs fit the emission depth model because subsurface layers will be warmer than the surface on desert nights when there is rapid surface cooling. Finally, the mean TB varies with frequency much more in the sandy case than the rocky case. Although emissivity differences may be partially responsible for this, the thermal model provides two possible explanations: (1) diurnal cycle asymmetry may change with $\alpha$ and shift the apparent mean of a two-point diurnal cycle sample or (2) there may be longer-term, depth-dependent variations in diurnal mean temperature (e.g., $T_0$ in equation (4)), e.g., due to seasonal cycles, that are only apparent with larger emission depths.

### 4.3. Land Surface Model Experiments

[36] Land surface model (LSM) simulations of the subsurface temperature profile can be used to show that typical TB spectral signatures can be explained by thermal conditions typical of dry surface types. We configured an LSM with coupled soil heat and moisture transport [*Galantowicz et al.*, 1999] for two surface materials: rock with relatively high thermal conductivity (3.0 W/mK) and lower conductivity dry sand (0.25 W/mK). We selected two Saharan grid points representing sand sea and rocky surface types (Figures 9 and 10) and estimated emitting temperatures from July 2003 atmospherically corrected AMSR-E TBs and time series method emissivities by inversion of equation (2) for $T_e$. The month-average day-night differences were then computed for 11, 19, 37, and 89 GHz ($\Delta T_e$) and MODIS LSTs ($\Delta T_s$) (Table 1). For each surface type, LSM temperature profiles

**Table 1.** July 2003 Month Average Day-Night Temperature Differences (K), Sandy (25°N, 13°E) and Rocky (28°N, 3°E) Desert Locations

| Surface Type | AMSR-E Emitting Temperature $\Delta T_e$ | | | | MODIS LST $\Delta T_s$ |
|---|---|---|---|---|---|
| | 11 GHz | 19 GHz | 37 GHz | 89 GHz | |
| Sandy | 2.1 | 2.7 | 4.6 | 9.8 | 28.8 |
| Rocky | 13.8 | 17.0 | 21.1 | 25.5 | 25.6 |

**Table 2.** Averaging Depths (cm) at Which $\Delta T_{avg} = \Delta T_e$ From Table 1

| Surface Type | Averaging Depth for $\Delta T_{avg} = \Delta T_e$ | | | |
|---|---|---|---|---|
| | 11 GHz | 19 GHz | 37 GHz | 89 GHz |
| Sandy | 61 | 48 | 29 | 16 |
| Rocky | 18 | 12 | 6 | 0 |

(31 layers to 1 m depth) were simulated from a 15 day model run with prescribed diurnal solar and atmospheric forcing parameters. Air temperature diurnal amplitude and wind speed were tuned so that the skin temperature change from 01:30 to 13:30 on the last model day closely matched $\Delta T_s$ from the MODIS LST. The 01:30–13:30 simulated temperature change was calculated over the entire profile ($\Delta T(z)$) and then normalized for an exact match between modeled $\Delta T(z = 0)$ and $\Delta T_s$ from the MODIS: $\Delta T'(z) = \Delta T(z) \cdot \Delta T_s / \Delta T(z = 0)$. This normalization facilitates direct comparisons between modeled and observed temperature changes, and does not affect the generality of the analysis since we are only comparing the relative day-night change between model levels and are not testing the ability of the model to simulate the absolute temperatures observed. Finally, a depth-average profile ($\Delta T_{avg}$) was calculated by averaging $\Delta T'(z)$ from the surface to $z$ to approximate an emission source distributed over depth in a manner similar to equation (6).

[37] For each frequency and surface type, we found the depth (Table 2) at which the 01:30/13:30 $\Delta T_{avg}$ matched the estimated microwave emission temperature change (Table 1). Figure 11 illustrates this process graphically. For example, the 11 GHz $\Delta T_e$ for sandy desert (2.1 K) corresponds to the simulated $\Delta T_{avg}$ at 61 cm and for rock $\Delta T_e$ (13.8 K) corresponds to 18 cm. A similar analysis by

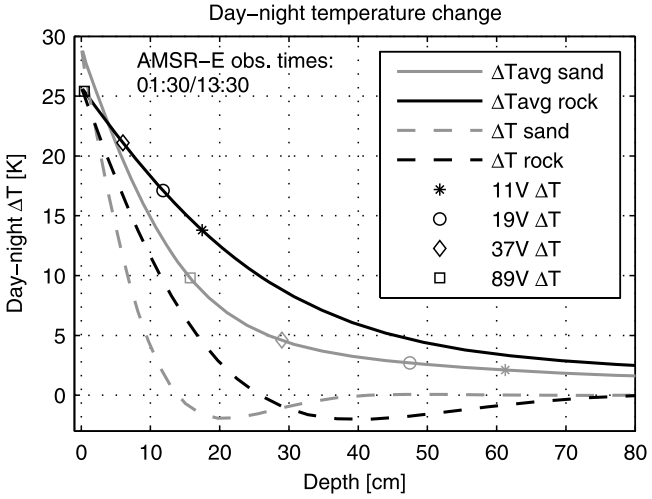


**Figure 11.** LSM day-night temperature change ($\Delta T$, dashed lines) and $\Delta T$ averaged over depth ($\Delta T_{avg}$ solid lines) at the AMSR-E nominal observation times for sand (gray lines) and rock (black lines) surface types. AMSR-E $\Delta T_e$ for 11, 19, 37, and 89 GHz estimated at the same location (July 2003 average) from V polarization data are plotted to show graphically the depth at which they correspond to $\Delta T_{avg}$.

**Table 3.** MEDI Estimated From Averaging Depths in Table 2

| Surface Type | MEDI From Averaging Depths | | | |
|---|---|---|---|---|
| | 11 GHz | 19 GHz | 37 GHz | 89 GHz |
| Sandy | 9.2 | 7.2 | 4.4 | 2.4 |
| Rocky | 1.0 | 0.7 | 0.3 | 0 |

Prigent99 estimated depths up to 15 cm at 19 GHz. From these depths and the LSM thermal diffusivity (1.6E-7 and 1.2E-6 $m^2/s$ for sand and rock, respectively) we can estimate MEDI as $\alpha = d\sqrt{\omega_0/2\kappa}$ (Table 3). These values are consistent with the retrieved 11 GHz MEDI range across the Sahara (Figure 2), where a mixture of surface media can be expected even in relatively homogeneous regions. Furthermore, the sandy-case MEDI estimates correspond well to the upper range of retrieved MEDI at each frequency (Figure 2).

[38] LSM-simulated subsurface temperature profiles and the emission depths inferred from AMSR-E data can be

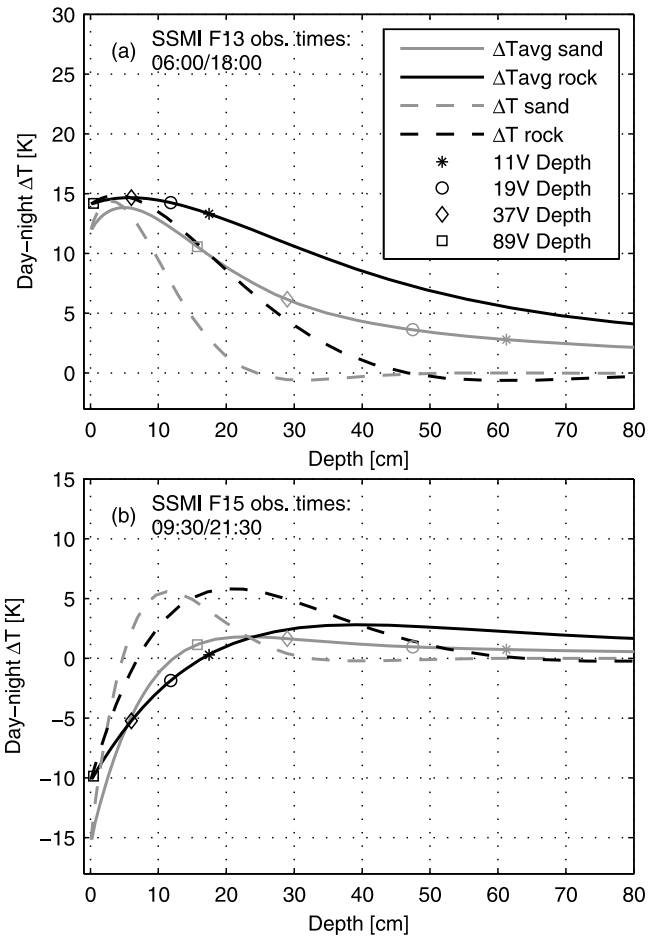


**Figure 12.** Similar to Figure 11 but for the (a) SSM/I F13 and (b) F14 nominal observation times. In Figure 11, the marker placement along the curves indicates the use of AMSR-E-derived $\Delta T_e$ to estimate depths, while in this plot those depths are used to graphically estimate $\Delta T_e$ at the SSM/I observations times with the aid of the corresponding LSM $\Delta T_{avg}$.

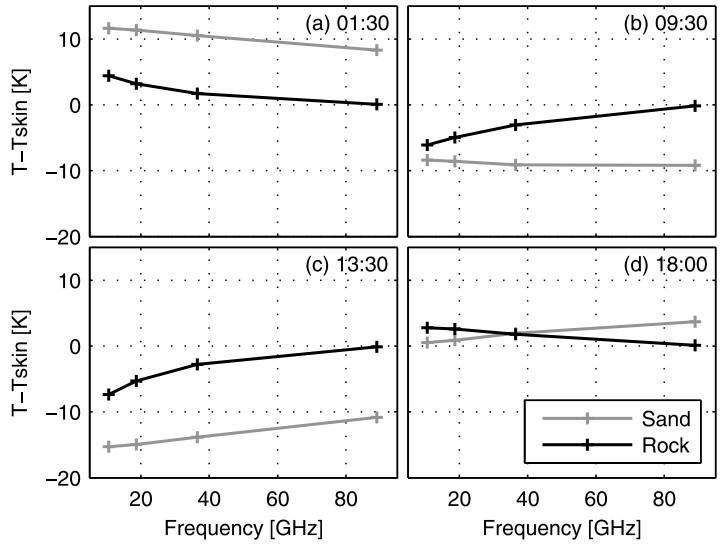


**Figure 13.** LSM depth-average temperature relative to skin temperature, $T_{avg}$-$T_s$, versus microwave frequency inferred using emission depths estimated from AMSR-E analysis (Figure 11) at four LSM times: (a) 01:30 (AMSR-E), (b) 09:30 (F15), (c) 13:30 (AMSR-E), and (d) 18:00 (F13).

used to examine how thermal gradients may affect TB day-night differences and spectra at different sampling times. For example, information in spectral gradients is used in retrieval algorithms for vegetation and soil moisture [e.g., *Njoku and Chan*, 2006], and time-of-day dependent crosstalk between spectral gradients due to subsurface temperature structure and emissivity can introduce errors when an algorithm assumes that emissivity is the primary effect. Similarly, a microwave land surface (skin) temperature retrieval algorithm may incur errors by assuming $T_e$ is frequency-independent. Unlike $\Delta T_{avg}$ at 01:30/13:30, which monotonically decreases with depth for both surface types, LSM-simulated $\Delta T_{avg}$ at the observation times of SSM/I F13 and F15 (06:00/18:00 and 09:30/21:30, respectively) are not monotonic and the spectral dependence of the day-night difference varies significantly (Figure 12). For instance, $\Delta T_{avg}$ is nearly uniform among all the measured frequencies for rock with F13 sampling and sand with F15 sampling, but in the first case $\Delta T_s \approx \Delta T_{avg}$ while in the second case $\Delta T_s \approx -15$ K and $\Delta T_{avg} \approx 2$ K. Diurnal sampling where $\Delta T_s \approx \Delta T_{avg}$ (rock/F13) would mask emission depth effects entirely while the sand/F15 case would reveal an overall emission depth effect but the frequency dependence would be masked. Because of emission depth masking, neither F13 nor F15 sampling alone would be sufficient for application of the time series emissivity retrieval method in these measurement conditions.

[39] $T_e$ spectral signatures (relative to $T_s$) inferred from $T_{avg}$ at various sampling times (Figure 13) illustrate how the sand and rock cases have different implications for LST retrieval. First, in both cases there is significant variation in the $T_e$ spectral gradient throughout the day even for cases where $\Delta T_{avg}$ was near constant (Figures 12 and 11), meaning that an LST retrieval algorithm would need to account for time-dependent $T_e$–$T_s$ differences to use data from frequencies at which emission depth was nonnegligible. Second, the sand-case $T_e$ spectral gradients are usually small relative to the $T_e$-$T_s$ difference, meaning that both $T_e$ retrieval precision and emission depth knowledge would need to be very good in order to accurately retrieve $T_s$ even where emissivities are well known. In contrast, the rock cases are better suited for LST retrieval since (1) emission depths and emissivities may be determined from time series analysis even without 01:30/13:30 sampling, (2) 89 GHz emission depth is near zero, and (3) the $T_e$ spectral gradients are large relative to the $T_e$-$T_s$ difference so that even less precise $T_e$ estimates at lower frequencies (which are less affected by atmospheric noise than 89 GHz) can be useful in LST retrievals.

## 5. Conclusion

[40] Retrievals based on time series analysis of brightness temperatures show that variations in an index of microwave emission depth (MEDI) are measurable in areas worldwide, and not only in the arid, barren regions where subsurface emission effects have been detected in previous studies (e.g., Prigent99). Small annual variation in MEDI and emissivity in some regions and the lack of a strong dependence of MEDI on latitude indicate that the retrieval method is robust to differences in diurnal thermal forcing. Where seasonal changes do occur, examples show that they correspond to monthly changes in vegetation amount and surface wetness, i.e., factors that are expected to affect transmittance in the surface medium as well as its emissivity. A case study comparing seasonal change in northern and southern Africa provided evidence that 11 GHz MEDI may be sensitive to land surface moisture and vegetation changes during multimonth dry spells whereas emissivities may be more sensitive to vegetation alone. It may be possible to improve surface parameter retrieval algorithms for arid regions by exploiting these complimentary surface moisture and vegetation sensitivities.

[41] Several tests performed with the retrieval products, raw data, and simulations validate the underlying assumptions of the method and rule out other possible causes of the day-night patterns observed, including horizontal heterogeneity. The retrieval model's low fit error (2 to 3 K) at all four

microwave frequencies and across various surface types provides evidence that the model is applicable even where the assumption of a homogeneous, flat soil surface is violated (e.g., due to vegetation cover). Tests showed that surface type (and not, for instance, hypothetical AMSR-E calibration errors induced by scene temperature or time of day) is the main factor driving systematic day-night differences. The day-night and spectral signatures observed at sites with moderate-transmittance (rock) and higher-transmittance (dry sand) surfaces are consistent with simulated subsurface temperature profiles from a land surface model (LSM), verifying that the simplified thermal model in the time series retrieval method can yield results similar to more complex thermal modeling based on first principles. LSM simulations showed that sampling time of day strongly affects the ability to (1) detect and estimate emission depth from time series data and (2) retrieve land surface skin temperature from microwave-only data where emission depth is significant. AMSR-E sampling (01:30/13:30 equator crossing times, when near-surface temperature gradients are likely to be large) is more effective for emission depth estimation than either SSM/I F13 (06:30/18:30) or F15 (21:00/09:00) sampling alone. However, the time series retrieval method relies on complete sampling of the diurnal cycle to define phase and so should benefit from the inclusion of additional similar-quality microwave and LST measurements, as available. Methods for adapting the retrieval's analysis interval to the shortest period in which emissivity is stable and sufficient clear-sky samples are available will help to further evaluate the usefulness of MEDI as an indicator of subsurface moisture or vegetation amount in arid and semiarid regions.

[42] **Acknowledgment.** This paper is based upon work supported by the National Aeronautics and Space Administration under contract NNH04CC43C issued through the Science Mission Directorate.

## References

Ashcroft, P., and F. Wentz (2006), AMSR-E/Aqua L2A Global Swath Spatially Resampled Brightness Temperatures V09, January to December 2003, accessed 14 November 2009, http://nsidc.org/data/daac/ae_l2a_tbs.gd.html, Natl. Snow and Ice Data Cent., Boulder, Colo. [updated daily]

Friedl, M. A., et al. (2002), Global land cover mapping from MODIS: Algorithms and early results, *Remote Sens. Environ.*, *83*, 287–302, doi:10.1016/S0034-4257(02)00078-0.

Galantowicz, J. F., D. Entekhabi, and E. G. Njoku (1999), Tests of sequential data assimilation for retrieving profile soil moisture and temperature from observed L band radiobrightness, *IEEE Trans. Geosci. Remote Sens.*, *37*, 1860–1870, doi:10.1109/36.774699.

Grody, N. C., and F. Weng (2008), Microwave emission and scattering from deserts: Theory compared with satellite measurements, *IEEE Trans. Geosci. Remote Sens.*, *46*, 361–375, doi:10.1109/TGRS.2007.909920.

Huete, A., K. Didan, T. Miura, E. P. Rodriguez, X. Gao, and L. G. Ferreira (2002), Overview of the radiometric and biophysical performance of the MODIS vegetation indices, *Remote Sens. Environ.*, *83*, 195–213, doi:10.1016/S0034-4257(02)00096-2.

Kunkee, E. B., G. A. Poe, D. J. Boucher, S. D. Swadley, Y. Hong, J. E. Wessel, and E. A. Uliana (2008), Design and evaluation of the first Special Sensor Microwave Imager/Sounder, *IEEE Trans. Geosci. Remote Sens.*, *46*, 863–883, doi:10.1109/TGRS.2008.917980.

Moncet, J.-L., P. Liang, J. F. Galantowicz, A. E. Lipton, G. Uymin, C. Prigent, and C. Grassotti(2011a), Land surface microwave emissivities derived from AMSR-E and MODIS measurements with advanced quality control, *J. Geophys. Res.*, doi:10.1029/2010JD015431, in press.

NASA (2009a), TRMM and Other Sources Rainfall Product (TRMM Product 3B43), http://mirador.gsfc.nasa.gov/collections/TRMM_3B43__006.shtml, accessed 7 December 2009, NASA Goddard Space Flight Cent., Greenbelt, Md.

NASA (2009b), Vegetation Index [NDVI](1 month-Terra/MODIS), NASA Earth Observations (NEO), http://neo.sci.gsfc.nasa.gov/Search.html?group=24, accessed 7 December 2009, NASA Goddard Space Flight Cent., Greenbelt, Md.

Njoku, E. G., and S. K. Chan (2006), Vegetation and surface roughness effects on AMSR-E land observations, *Remote Sens. Environ.*, *100*, 190–199, doi:10.1016/j.rse.2005.10.017.

Prigent, C., W. B. Rossow, and E. Matthews (1997), Microwave land surface emissivities estimated from SSM/I observations, *J. Geophys. Res.*, *102*, 21,867–21,890, doi:10.1029/97JD01360.

Prigent, C., W. B. Rossow, E. Matthews, and B. Marticorena (1999), Microwave radiometer signatures of different surface types in deserts, *J. Geophys. Res.*, *104*, 12,147–12,158, doi:10.1029/1999JD900153.

Prigent, C., F. Aires, and W. B. Rossow (2006), Land surface microwave emissivities over the globe for a decade, *Bull. Am. Meteorol. Soc.*, *87*, 1573–1584, doi:10.1175/BAMS-87-11-1573.

Rossow, W. B., and R. A. Schiffer (1999), Advances in understanding clouds from ISCCP, *Bull. Am. Meteorol. Soc.*, *80*, 2261–2287, doi:10.1175/1520-0477(1999)080<2261:AIUCFI>2.0.CO;2.

Ulaby, F. T., R. K. Moore, and A. K. Fung 1986: *Microwave Remote Sensing: Active and Passive: Volume III: From Theory to Applications*, Artech House, Norwood, Mass., pp. 2082–2104.

Wan, Z. (1999), MODIS land-surface temperature algorithm theoretical basis document (LST ATBD), version 3.3, http://modis.gsfc.nasa.gov/data/atbd/atbd_mod11.pdf, report, NASA Goddard Space Flight Cent., Greenbelt, Md.

Wan, Z. (2008), New refinements and validation of the MODIS land-surface temperature/emissivity products, *Remote Sens. Environ.*, *112*, 59–74, doi:10.1016/j.rse.2006.06.026.

Wentz, F., and T. Meissner (1999), AMSR ocean algorithm: Algorithm theoretical basis document (ATBD), version 2, *RSS Tech. Prop. 121599A*, Remote Sens. Syst., Santa Rosa, Calif.

J. F. Galantowicz, P. Liang, A. E. Lipton, J.-L. Moncet, and G. Uymin, Atmospheric and Environmental Research, Inc., 131 Hartwell Ave., Lexington, MA 02421-3126, USA. (johng@aer.com)

C. Grassotti, I.M. Systems Group, Center for Satellite Applications and Research, NESDIS, NOAA, 5200 Auth Rd., Rm. 712, Camp Springs, MD 20746, USA.

C. Prigent, Laboratoire d'Etudes du Rayonnement et de la Matière en Astrophysique, Observatoire de Paris, CNRS, Paris, France.